

# Ab initio study on the possible magnetic topological semimetallic state in $\text{MnMg}_2\text{O}_4$

Satoshi Tomita,<sup>1</sup> DaPeng Yao,<sup>2</sup> Hiroki Tsuchiura,<sup>1, a)</sup> and Kentaro Nomura<sup>3, a)</sup>

<sup>1)</sup>Department of Applied Physics, Tohoku University, Sendai 980-8579, Japan

<sup>2)</sup>Department of Physics, Tokyo Institute of Technology, Tokyo 152-8551, Japan

<sup>3)</sup>Institute for Materials Research, Tohoku University, Sendai 980-8577, Japan

(\*Electronic mail: hiroki.tsuchiura.e8@tohoku.ac.jp .)

(Dated: 20 January 2022)

We study the electronic state of an inverse spinel compound  $\text{MnMg}_2\text{O}_4$  based on first-principles calculations. The high-spin state is realized in Mn ions on the diamond lattice, resulting in that this material is found to be a half-metallic semimetal with the minority spin-gap about 3eV, and also with line nodes in the Brillouin zone. The intrinsic anomalous Hall conductivity (AHC) is also computed as a function of the chemical potential of the system assuming the rigid band structure, and is found to exhibit a peak structure with a maximum value of 200 S/cm at only 15 meV above the Fermi level. The relation between the large AHC and Berry curvature in the Brillouin zone is also discussed.

## I. INTRODUCTION

Topological semimetals, such as Weyl semimetals, are in a class of gapless electronic phases that exhibit topologically stable crossings of energy bands. In these materials, Berry curvature emerging within the band structure near the Fermi energy acts like a magnetic field in momentum space, resulting in robust bulk transverse transport against disorder. It provides novel degrees of freedom in spintronic applications or thermoelectric energy conversion. Thus the search for topological semimetals has been one of the most intriguing issues in the field of spintronics.

Theoretically, a spinel compound  $\text{HgCr}_2\text{Se}_4$  was the first to be predicted to be a magnetic Weyl semimetal<sup>1</sup>. Several years later, soon after the experimental confirmation of a theoretical prediction that TaAs is a nonmagnetic Weyl semimetal<sup>2</sup>, a few magnetic materials such as a shandite compound  $\text{Co}_3\text{Sn}_2\text{S}_2$  and the (inverse) Heusler compounds  $\text{Co}_2\text{MnAl}$  and  $\text{Ti}_2\text{MnAl}$  were theoretically predicted to be magnetic Weyl semimetals, some of which were confirmed experimentally<sup>3-8</sup>.

Quite recently, the inverse spinel compound  $\text{VMg}_2\text{O}_4$  has been predicted to be an excellent topological semimetal with the so-called hourglass-shaped band dispersion based on an effective tight-binding model and also on first-principles calculations<sup>9,10</sup>. The hourglass-shaped band dispersion is formed on the  $e_g$  band consisting of V 3d orbitals on the diamond lattice, which is fully polarized and well separated from the other bands. It is also found that  $\text{VMg}_2\text{O}_4$  becomes a magnetic Weyl semimetal when the spin-orbit interaction is taken into account. Since spinel compounds have been widely studied from various aspects in the field of spintronics, for example, the application of a nonmagnetic spinel  $\text{MgAl}_2\text{O}_4$  as a tunneling barrier of tunnel magneto-resistance device<sup>11,12</sup>, and the utilization of strain-induced high magnetic anisotropy in  $(\text{CoFe})_2\text{O}_4$  ferrite<sup>13</sup>, the search for new topological semimetals by shedding the light of topological

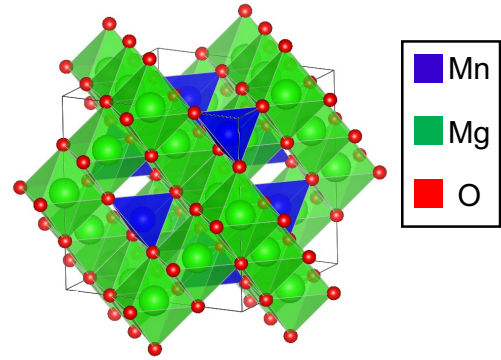


FIG. 1. Conventional unit cell for  $\text{MnMg}_2\text{O}_4$ .

physics on spinel compounds may open the door to the invention of novel spintronic devices.

Let us now look at the 3d electronic states of  $\text{VMg}_2\text{O}_4$ . If each V ion maintains the nominal  $\text{V}^{4+}$  charge, then it has one electron on the  $e_g$ -orbitals. In a tight-binding picture, this corresponds to the situation where there is one electron per each site of the diamond lattice which consists of two degenerate orbitals. Here we may ask what happens if we consider a similar situation with  $t_{2g}$ -orbitals. Such a situation can be realized in  $\text{MnMg}_2\text{O}_4$  in which V is totally substituted for Mn. If the high-spin state is realized in the tetravalent configuration of Mn ions, there is one electron in the  $t_{2g}$ -orbitals. Thus, we can expect that this system is a  $t_{2g}$  counterpart of  $\text{VMg}_2\text{O}_4$ .

In this paper, we study the electronic state of  $\text{MnMg}_2\text{O}_4$ , and examine the topological nature of the transverse transport properties of this system by calculating the intrinsic anomalous Hall conductivity (AHC) and the electronic Berry curvature over the occupied portions of the Brillouin zone based on first-principles calculations.

<sup>a)</sup>Also at Center for Spintronics Research Network, Tohoku University, Sendai 980-8577, Japan.

## II. COMPUTATIONAL DETAILS

To investigate the electronic band structure of  $\text{MnMg}_2\text{O}_4$ , we have performed *ab initio* calculations based on density functional theory (DFT) using the full-potential linearized-augmented plane-wave (FP-LAPW) method as implemented in the WIEN2k code<sup>14</sup>. Our calculations are based on generalized gradient approximation using the exchange-correlation functional proposed by Perdew, Burke and Ernserhof (PBE-GGA)<sup>15</sup>. We used the value of  $R_{\text{MT}}K_{\text{max}} = 7$  in this study, where  $R_{\text{MT}}$  means the muffin tin sphere radius and  $K_{\text{max}}$  means the largest wave vector. The muffin tin sphere was chosen to be  $R_{\text{MT}}^{(\text{Mn})} = 2.00$  a.u.,  $R_{\text{MT}}^{(\text{Mg})} = 1.50$  a.u., and  $R_{\text{MT}}^{(\text{O})} = 1.20$  a.u.. For SCF calculations, we used the -mesh of size  $10 \times 10 \times 10$   $k$ -points obtained by Monkhorst-Pack sampling method<sup>16</sup> and energy convergence criteria were set as  $10^{-6}$  Ry.

To evaluate the transverse transport property of  $\text{MnMg}_2\text{O}_4$ , we calculated AHC ( $\sigma_{xy}$ ) from following Kubo formula

$$\sigma_{xy} = \frac{1}{(2\pi)^3} \sum_n \int_{\text{BZ}} dk f(E_{nk}) \Omega_n^z(k), \quad (1)$$

$$\Omega_n^z(k) = -\frac{ie^2}{\hbar} \sum_{m(\neq n)} \frac{\langle u_{n,k} | v_x | u_{m,k} \rangle \langle u_{m,k} | v_y | u_{n,k} \rangle - \text{c.c.}}{(E_n(k) - E_m(k))^2}, \quad (2)$$

where  $f(E_{n,k})$  is Fermi-Dirac distribution function,  $\Omega^z$  is  $z$  component of Berry curvature, and  $v_i (i = x, y)$  are velocity operators. To perform BZ integration, we adopted finer  $k$ -mesh of size  $60 \times 60 \times 60$   $k$ -points. For a deeper understanding of topological nature of  $\text{MnMg}_2\text{O}_4$ , we analyzed effective model obtained by maximally localized generalized Wannier functions (MLWF)<sup>17</sup> based on the results of DFT calculations. MLWFs were constructed to reproduce DFT results by using WIEN2WANNIER package<sup>18</sup> and WANNIER90 package<sup>19</sup>. Based on MLWF, we analyzed distribution of nodes and Berry curvature in  $k$ -space by using WANNIERTOOLS package<sup>20</sup>.

We studied bulk  $\text{MnMg}_2\text{O}_4$  with inverse-spinel structure, whose conventional crystal structure is shown in Fig. 1, which was produced with VESTA<sup>21</sup>. The crystal structure belongs to a face-centered cubic Bravais lattice with space group Fd3m (No.227). As shown in Fig. 1, Mn atom is surrounded by four O atoms, which acts as tetrahedral field. We performed optimization to obtain lattice constant and internal atomic positions. The optimized lattice constant is  $a = b = c = 8.380$  Å. Among 56 atoms  $\text{MnMg}_2\text{O}_4$  in a unit cell, Mn atoms locate at  $8a(0.125, 0.125, 0.125)$  Wyckoff positions, Mg atoms locate at  $16d(0.500, 0.500, 0.500)$  Wyckoff positions, and O atoms locate at  $32e(0.251, 0.251, 0.251)$  Wyckoff positions, where we chose origin choice 2. These values are used in DFT calculations.

## III. RESULTS

First, we show the band structure of  $\text{MnMg}_2\text{O}_4$  along the main symmetry directions in Fig. 2 (a). It can be clearly seen that the energy bands near the Fermi level are all in the spin-up channel. We also show the orbital projected density of states

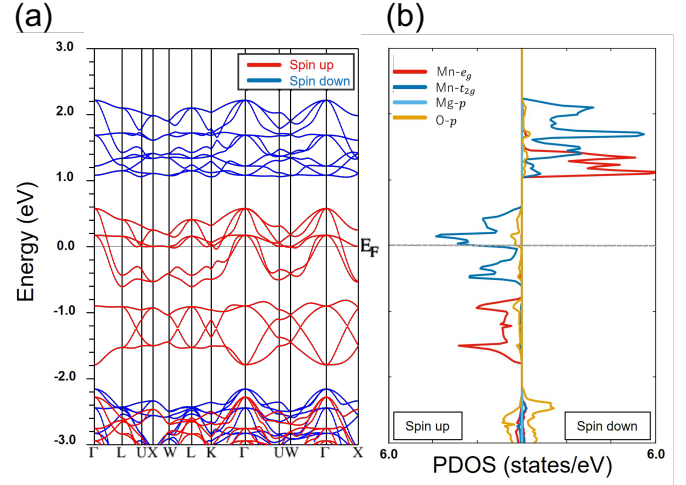


FIG. 2. Calculated (a) electronic band structures and (b) partial density of states for Mn  $e_g$  and  $t_{2g}$ , Mg  $2p$ , and O  $2p$  orbitals in  $\text{MnMg}_2\text{O}_4$ .

(DOS) in majority-spin (positive) and minority-spin (negative) channels in Fig. 2 (b). Now the semimetallic feature with an about 3eV minority spin gap of  $\text{MnMg}_2\text{O}_4$  is clearly noticeable. One can see that the energy band crossing the Fermi level mainly consists of  $t_{2g}$  orbitals of Mn 3d-electrons. Also, the fully spin-polarized  $e_g$ -band with the hourglass dispersion is found about 1eV below the Fermi level. The results shown in Fig. 2 confirm our expectation that the high-spin state is realized in  $\text{MnMg}_2\text{O}_4$ .

In Fig. 2, We also notice the doubly degenerate bands with a very flat dispersion along the  $X - W$  symmetry line just above the Fermi energy. Since it is known that topological line nodes appear along the  $X - W$  path in the single-orbital diamond lattice, we can expect that these degenerate bands can be a manifestation of such nodal lines in this system. Thus, it is interesting to look at the energy gap between these two bands near the  $X - W$  symmetry lines in the Brillouin zone. The first Brillouin zone of the system is shown in Fig. 3 (a); the three square  $k$ -planes bordered by blue, red, green lines are the (001), (100), and (010) surfaces at the Brillouin zone edge, respectively. These  $k$ -planes contain the  $X - W$  symmetry lines as shown in Fig. 3 (b). We show the energy gap between the two entangled bands on these  $k$ -planes obtained without and with the spin-orbit interaction in Fig. 3 (c) and (d). In the absence of the spin-orbit interaction, these three  $k$ -planes are equivalent, and the system has two equivalent nodal lines crossing each other on each of the planes, as shown in Fig. 3 (c). On the other hand, if we take into account the spin-orbit interaction and let the magnetization direction be (001), the three  $k$ -planes are no longer equivalent, and only one nodal line remains on the (100) and (010) planes, as shown in Fig. 3 (d). Thus we confirm that  $\text{MnMg}_2\text{O}_4$  is approximately a nodal line semimetal.

Next, let us look at the intrinsic AHC  $\sigma_{xy}$  as a function of the chemical potential of the system when the magnetization is along the [001] axis, assuming a rigid band structure.

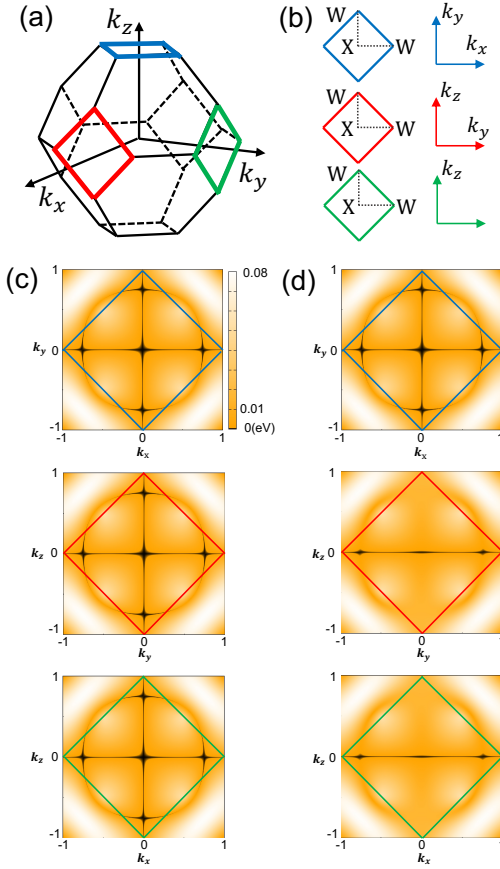


FIG. 3. (a) First Brillouin zone (BZ) of the inverse spinel structure shown in Fig. 1. The three square  $k$ -planes bordered by blue, red, green lines are the (001), (100), and (010) surfaces at the Brillouin zone edge, respectively. The  $X-W$  symmetry lines on these surfaces are depicted in (b). The energy gap between the two entangled bands on these planes calculated without and with the spin-orbit interaction is shown in (c) and (d), respectively. The blue, red, green borders in (c) and (d) correspond to those in (b).

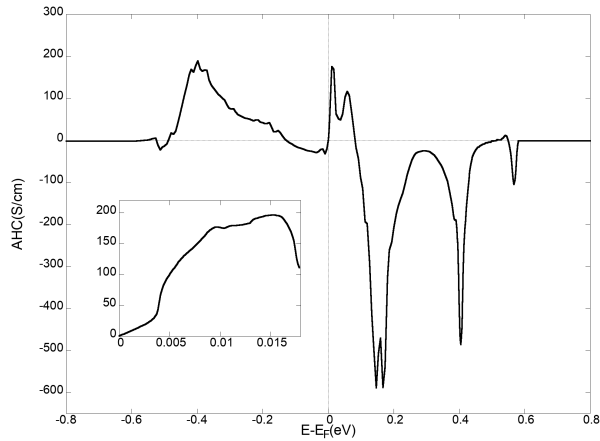


FIG. 4. Chemical potential dependence of calculated AHC. The inset shows the detailed plot of AHC in the range of  $E = 0-0.018$  eV.

We compute the intrinsic AHC using the Kubo formula in the clean limit. We use a finer  $k$ -mesh with 14671  $k$ -points within the reduced Brillouin zone for the AHC calculation using the OPTIC module in WIEN2k code. In Fig. 4, we show the result of the AHC as a function of the chemical potential. Although the intrinsic AHC is only 0.8 S/cm on the Fermi level, it increases sharply with slightly increasing the chemical potential from  $E_F$ , then the AHC shows a peak value of  $\sigma = 200$  S/cm at  $E - E_F = 0.015$  eV, as seen in the inset of Fig. 4.

It is tempting to think here that the large AHC at around  $E - E_F = 0.015$  eV is due to the topological nature of the nodal lines found in Fig. 2. Thus finally, we analyze the Berry curvature distribution on the  $k$ -planes defined in Fig. 3 to confirm the effects of the nodal lines on the AHC. Figure 5 (a) shows

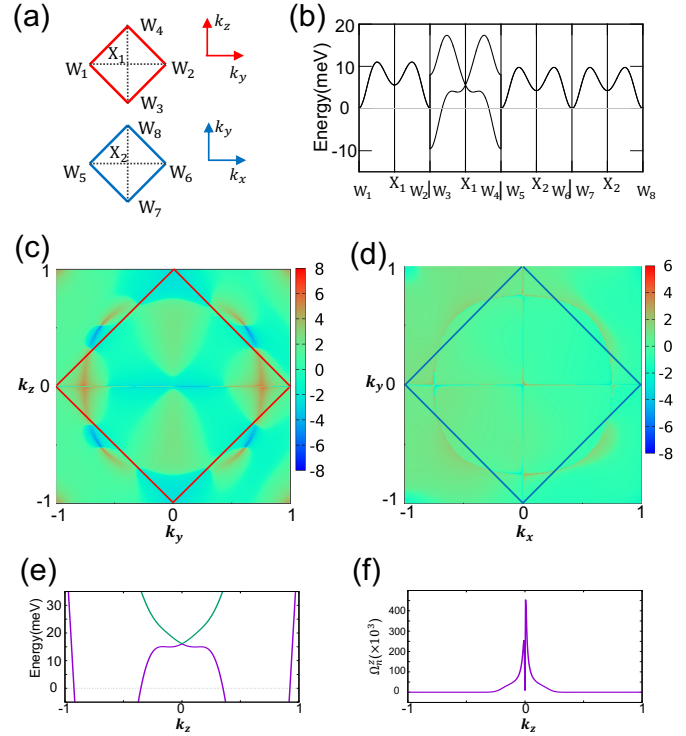


FIG. 5. (a) The (100) and (001)  $k$ -planes as in the same manner in Fig. 3 (b). (b) The energy dispersion on  $X-W$  symmetry lines, where the labels of symmetry points are given in (a). The Berry curvature on the (100) and (001)  $k$ -planes are shown in (c) and (d), respectively. In (c) and (d), the magnitude of the  $z$  component of the Berry curvature is plotted in a logarithmic scale  $\text{sign}(\Omega_n^z) * (1 + \log_{10}(\Omega_n^z))$ . (e) The band dispersion along  $k_y = 0.75$  near the (100)  $k$ -plane. (f) Calculated Berry curvature along  $k_y = 0.75$  on the (100)  $k$ -plane.

the (100) and (001)  $k$ -planes as in the same manner in Fig. 3 (a) and (b). As mentioned earlier, if the magnetization of the system is along the [001] direction, the electronic states of these two planes are not equivalent due to the effect of spin-orbit interaction. Thus for clarity, we here distinguish the  $X$  and  $W$  points which were originally equivalent with subscripts as in Fig. 5 (a). A detailed view of the band dispersion along the symmetry lines on these planes is shown in Fig. 5 (b).

The narrow energy band is found to be in the range of -10 to 18meV, which coincides with the peak value of the AHC. Furthermore, we find the hot spots of the Berry curvature around  $k_y \simeq \pm 0.75$  on the nodal line on the (100)  $k$ -plane as shown in Fig. 5 (c). Note here that no hot spots or prominent features are found in the calculated Berry curvature on the (001)  $k$ -plane as can be seen from Fig. 5 (d). Let us take a closer look at the band structure and the Berry curvature distribution around the hot spots. Figure 5 (e) and (f) shows the band dispersion along  $k_y = 0.75$  near the (100)  $k$ -plane. A nearly flat portion of the band with a band crossing at  $k_z = 0$  lies around  $E = 0.015\text{eV}$ , which coincides again with the peak value of the AHC in Fig. 4. The calculated Berry curvature along  $k_y = 0.75$  on the (100)  $k$ -plane is also shown in Fig. 5 (f). We notice that the Berry curvature is large in the flat portion of the band and exhibits strong peaks close to the crossing point. It should be noted here that the Berry curvature is almost zero at  $k_z = 0$ , i.e. on the nodal line. Therefore, we may conclude that the large AHC found at  $E \sim 0.015\text{eV}$  is not attributed to the nodal lines themselves, but to the hot spots found in very close proximity to them. More detailed studies on the origin of the hot spots and their topological nature will be reported in a forthcoming paper.

#### IV. SUMMARY

In summary, we have investigated the electronic states and the AHC in the inverse spinel compound  $\text{MnMg}_2\text{O}_4$  based on first-principles calculations, stimulated by the recent theoretical works of  $\text{VMg}_2\text{O}_4$ . The results have confirmed that this material is a half-metallic semimetal with the line nodes slightly above the Fermi level, and also exhibits fairly large AHC. The Berry curvature distribution near the nodal lines in the Brillouin zone has been also studied, and no direct relationship between the large AHC and the nodal lines was found. Instead, the hot spots of Berry curvature are found in very close proximity to the nodal lines. Future work is required to reveal the topological nature of the hot spots and the origin of the large AHC.

#### ACKNOWLEDGMENTS

This work was supported by JSPS KAKENHI Grant Number JP21H01025 and JP20H01830, and also by JST CREST Grant Number JPMJCR17J5 and JPMJCR18T2. Some numerical computations were carried out at the Cyberscience

Center, Tohoku University, Japan.

#### DATA AVAILABILITY

The data that support the findings of this study are available from the corresponding author upon reasonable request.

- <sup>1</sup>G. Xu, H. Weng, Z. Wang, X. Dai, and Z. Fang, Phys. Rev. Lett. **107**, 186806 (2011).
- <sup>2</sup>H. Weng, C. Fang, Z. Fang, B. A. Bernevig, and X. Dai, Phys. Rev. X **5**, 011029 (2015).
- <sup>3</sup>S.-Y. Xu, I. Belopolski, N. Alidoust, M. Neupane, G. Bian, C. Zhang, R. Sankar, G. Chang, Z. Uan, C.-C. Lee, S.-M. Huang, H. Zheng, J. Ma, D. S. Sanchez, B. Wang, A. Bansil, F. Chou, P. P. Shibayev, H. Lin, S. Jia, and M. Z. Hasan, Science **349**, 613 (2015).
- <sup>4</sup>Q. Xu, E. Liu, W. Shi, L. Muechler, J. Gayles, C. Felser, and Y. Sun, Phys. Rev. B **97**, 235416 (2018).
- <sup>5</sup>E. Liu, Y. Sun, N. Kumar, L. Muechler, A. Sun, L. Jiao, S.-Y. Yang, D. Liu, A. Liang, Q. Xu, J. Kroder, V. Süß, H. Borrmann, C. Shekhar, Z. Wang, C. Xi, W. Wang, W. Schnelle, S. Wirth, Y. Chen, S. T. B. Goennenwein, and C. Felser, Nat. Phys. **14**, 1125 (2018).
- <sup>6</sup>Q. Wang, Y. Xu, R. Lou, Z. Liu, M. Li, Y. Huang, D. Shen, H. Weng, S. Wang, and H. Lei, Nat. Commun. **9**, 3681 (2018).
- <sup>7</sup>P. Li, J. Koo, W. Ning, J. Li, L. Miao, L. Min, Y. Zhu, Y. Wang, N. Alem, C.-X. Liu, Z. Mao, and B. Yan, Nat. Commun. **11**, 3476 (2020).
- <sup>8</sup>W. Shi, L. Muechler, K. Manna, Y. Zhang, K. Koepernik, R. Car, J. van den Brink, C. Felser, and Y. Sun, Phys. Rev. B **97**, 060406 (2018).
- <sup>9</sup>W. Jiang, H. Huang, F. Liu, J.-P. Wang, and T. Low, Phys. Rev. B **101**, 121113 (2020).
- <sup>10</sup>H. Zhang, X. Zhang, T. He, X. Dai, Y. Liu, G. Liu, L. Wang, and Y. Zhang, Phys. Rev. B **102**, 155116 (2020).
- <sup>11</sup>H. Sukegawa, H. Xiu, T. Ohkubo, T. Furubayashi, T. Niizeki, W. Wang, S. Kasai, S. Mitani, K. Inomata, and K. Hono, Appl. Phys. Lett. **96**, 212505 (2010).
- <sup>12</sup>H. Sukegawa, Y. Miura, S. Muramoto, S. Mitani, T. Niizeki, T. Ohkubo, K. Abe, M. Shirai, K. Inomata, and K. Hono, Phys. Rev. B **86**, 184401 (2012).
- <sup>13</sup>T. Niizeki, Y. Utsumi, R. Aoyama, H. Yanagisawa, J.-I. Inoue, Y. Yamasaki, H. Nakao, K. Koike, and E. Kita, Appl. Phys. Lett. **103**, 162407 (2013).
- <sup>14</sup>P. Blaha, K. Schwarz, G. K. H. Madsen, D. Kvasnicka, J. Luitz, R. Laskowski, F. Tran, and L. D. Marks, WIEN2k: An Augmented Plane Wave plus Local Orbitals Program for Calculating Crystal Properties (Vienna University of Technology, Austria, 2018).
- <sup>15</sup>J. P. Perdew, K. Burke, and M. Ernzerhof, Phys. Rev. Lett. **77**, 3865 (1996).
- <sup>16</sup>H. J. Monkhorst and J. D. Pack, Phys. Rev. B **13**, 5188 (1976).
- <sup>17</sup>N. Marzari, A. A. Mostofi, J. R. Yates, I. Souza, and D. Vanderbilt, Rev. Mod. Phys. **84**, 1419 (2012).
- <sup>18</sup>J. Kuneš, R. Arita, P. Wissgott, A. Toschi, H. Ikeda, and K. Held, Comput. Phys. Commun. **181**, 1888 (2010).
- <sup>19</sup>G. Pizzi, V. Vitale, R. Arita, S. Blügel, F. Freimuth, G. Géranton, M. Gibertini, D. Gresch, C. Johnson, T. Koretsune, J. Ibañez-Azpiroz, H. Lee, J.-M. Lihm, D. Marchand, A. Marrazzo, Y. Mokrousov, J. I. Mustafa, Y. Nohara, Y. Nomura, L. Paulatto, S. Poncé, T. Ponweiser, J. Qiao, F. Thöle, S. S. Tsirkin, M. Wierzbowska, N. Marzari, D. Vanderbilt, I. Souza, A. A. Mostofi, and J. R. Yates, J. Phys.: Condens. Matter **32**, 165902 (2020).
- <sup>20</sup>Q. Wu, S. Zhang, H.-F. Song, M. Troyer, and A. A. Soluyanov, Comput. Phys. Commun. **224**, 405 (2018).
- <sup>21</sup>K. Momma and F. Izumi, J. Appl. Cryst. **44**, 1272 (2011).